On the Optical Response of Tellurium Activated Zinc Selenide ZnSe:Te Single Crystal

Dionysios Linardatos [1] , **Anastasios Konstantinidis** [2], **Ioannis Valais** [1] , **Konstantinos Ninos** [3], **Nektarios Kalyvas** [1] , **Athanasios Bakas** [3], **Ioannis Kandarakis** [1], **George Fountos** [1] **and Christos Michail** [1,*]

[1] Department of Biomedical Engineering, Radiation Physics, Materials Technology and Biomedical Imaging Laboratory, University of West Attica, Ag. Spyridonos, 12210 Athens, Greece; dlinardatos@uniwa.gr (D.L.); valais@uniwa.gr (I.V.); nkalyvas@uniwa.gr (N.K.); kandarakis@uniwa.gr (I.K.); gfoun@uniwa.gr (G.F.)

[2] Radiological Sciences Group, Department of Medical Physics, Portsmouth Hospitals University NHS Trust, Queen Alexandra Hospital, Portsmouth L8S 4L8, UK; Anastasios.Konstantinidis@porthosp.nhs.uk

[3] Department of Biomedical Sciences, University of West Attica, Ag. Spyridonos, 12210 Athens, Greece; kninos@uniwa.gr (K.N.); abakas@uniwa.gr (A.B.)

* Correspondence: cmichail@uniwa.gr; Tel.: +30-210-5385-387

Abstract: In this study, the light output of a zinc selenide activated with tellurium (ZnSe: Te) single crystal was measured for X-ray radiography applications. A cubic crystal ($10 \times 10 \times 10$ mm) was irradiated using X-rays with tube voltages from 50 to 130 kV. The resulting energy absorption efficiency, detective quantum efficiency, and absolute luminescence efficiency were compared to published data for equally sized GSO: Ce (gadolinium orthosilicate) and BGO (bismuth germanium oxide) crystals. The emitted light was examined to estimate the spectral compatibility with widely used optical sensors. Energy absorption efficiency and detective quantum efficiency of ZnSe: Te and BGO were found to be similar, within the X-ray energies in question. Light output of all three crystals showed a tendency to increase with increasing X-ray tube voltage, but ZnSe: Te stood at least 2 EU higher than the others. ZnSe: Te can be coupled effectively with certain complementary metal–oxide–semiconductors (CMOS), photocathodes, and charge-coupled-devices (CCD), as the effective luminescence efficiency results assert. These properties render the material suitable for various imaging applications, dual-energy arrays included.

Keywords: scintillators; crystals; radiation sensors; medical detectors; ZnSe: Te

1. Introduction

From its inception, medical imaging has undergone consistent advancements, with the X-ray imaging acquisition mechanism playing a fundamental part. In this respect, scintillating materials that convert X-rays to light photons, combined with a suitable means of detecting the latter ones, not only "survived" the rampant technological progress, but rather remain central for the scientific interest [1].

Most scintillating coatings are inorganic compounds of crystalline structure, solutions of organic compounds, or polymeric ones [2].

Out of several studies on these compositions over the years, it has been deduced that, in general, materials belonging to each group share certain specific characteristics. For example, inorganic alkali-halide crystals like sodium iodide (NaI: Tl) and cesium iodide (CsI: Tl) activated with thallium exhibit good light yield [3,4]. NaI: Tl is reportedly emitting 4.1×10^4 light photons per unit energy (MeV) of gamma-rays, while CsI: Tl emits 6.6×10^4 light photons per MeV of gamma-rays [5]. On the other hand, they exhibit large decay times and low radiation stability. Decay times of hundreds of nanoseconds (230 ns have

been measured by Hofstadter [6] regarding NaI: Tl) or even longer, at the microsecond range for CsI: Tl (0.8–6 μs reported by Grassmann et al. [7]). What's more, they are hygroscopic, NaI: Tl at a much greater extent, raising practical concerns in their application [8].

Oxide-based scintillators, like bismuth germanium oxide, $Bi_4Ge_3O_{12}$ (BGO), and gadolinium orthosilicate, Gd_2SiO_5: Ce (GSO: Ce), solve the problem of hygroscopicity and mechanical strength [9] offering high stopping power, yet at the cost of lower light yield in comparison with NaI: Tl. These materials have increased radiation absorption efficiency, density, and effective atomic numbers. BGO and GSO: Ce crystals have density values of 7.13 g/cm^3 and 6.7 g/cm^3, respectively, whereas CsI and NaI have 4.51 g/cm^3 and 3.67 g/cm^3 [10]. The corresponding effective atomic numbers are 74, 58, 54 and 56. A summary of the mechanical, optical and scintillation properties of the materials this paper pertains to, can be found in Table 1. Of decisive significance is the much faster decay time of GSO: Ce, 30 ns, which is only a fraction of the 300 ns of BGO and the 230 ns of NaI: Tl [9,11,12]. However, the two oxide-based scintillators show a strong deficiency in terms of light yield when compared to the two alkali-halide ones [10,13].

In an effort to overcome the limitations of the above-mentioned conventional materials, compounds belonging to the II–VI semiconductor group have been proposed and investigated. These compounds are comprised of a group II metal (e.g., zinc-Zn, cadmium-Cd, mercury-Hg) with a group VI cation (e.g., sulfur-S, selenium-Se, tellurium-Te) and characterized by a series of properties that render them suitable for use in medical imaging applications [14,15], namely good light output, rapid decay times, radiation and thermal stability, mechanical strength, and non-hygroscopicity [8]. A wide band-gap representative of these semiconductors, zinc selenide activated with tellurium (ZnSe: Te), has attracted the attention of several scientific teams, including ours, with the "first to obtain it" being Ryzhikov et al. [16]. In particular, this crystal has density 5.42 g/cm^3 and an effective atomic number of 33, thus implying a material at a comparable level of stopping power as the alkali-halides [16,17]. As for the light output, values vary within a broad interval, from $2.8 \cdot 10^4$ photons/MeV up to a maximum of 8×10^4 ph/MeV. In their analysis, Cool et al. [18] attribute this fact to the self-absorption within the material, something that depends on the quality of the specific crystal.

What seems indisputable is the material's short decay time. The latter ranges from 150 μs of "slow" versions of the crystal [8], down to 1 μs in polycrystalline film form, as shown by Gaysinskiy et al. [19]. Obviously, even in its "slowest" version, this material is particularly well-suited for use in high frame-rate radiography applications and CT.

The combination of high efficiency, low effective atomic number, and red light emission comes in beneficial contrast to the higher effective atomic numbers and different wavelength emissions of CsI: Tl, cadmium tungstate, $CdWO_4$, and gadolinium oxysulfide, Gd_2O_2S (GOS) [18]. Another convenient feature is its similar atomic number to that of copper; a widely used filter for the lower energy part of X-ray spectra. Thus, ZnSe: Te finds perfect application in dual energy detectors, incorporating it as the detecting element for the low energy photons. The high energy photons, after traversing this first layer, interact with a higher probability with one of the above-mentioned materials [16]. Such dual energy pairs enhance the capabilities of medical imaging, discriminating between muscular and osseous tissue, or between low-contrast structures, helping the diagnosis of tumors, osteoporosis, atherosclerosis, etc. [28–30]. Beyond the medical field, they are applied in baggage inspection equipment, high-energy physics, space probes, dosimetry, even in the quantum confinement regime (quantum dots) [8,31].

On the other hand, ZnSe single crystals are prone to re-crystallization and exhibit poor transparency. This limits their usable thickness, even though advanced single crystal growth techniques have enabled their use as radiation sensors [8].

Table 1. BGO, GSO:Ce, ZnSe:Te crystal properties [8–13,17,20–26].

Properties	BGO	GSO:Ce	ZnSe:Te
Wavelength, max emission (nm)	480	430	640
Wavelength Range (nm)	375–650	400–650	525–750
Decay Time	300 ns	30–60 ns	1–150 μs
Afterglow	0.05% @ 3ms	0.005% @ 6ms	< 0.05% @ 6ms
Light Yield (photons/MeV)	$8.9 \cdot 10^3$	$8.0 \cdot 10^3$	$2.8\text{–}16.9 \cdot 10^4$ $(4 \cdot 10^4)^a$
Photoelectron Yield (% of NaI:Tl)	15–20	20	31.5–63
Radiation Length (cm)	1.12	1.38	2.23
Refractive Index	2.15 @ 480 nm	1.85	2.67 @ 550 nm
Density (g/cm^3)	7.13	6.7	5.42
Effective Atomic Number	74	58	33
Melting Point (°C)	1044	1627	1779
Thermal Expansion Coefficient (°C^{-1})	$7.0 \cdot 10^{-6}$	$4\text{–}12 \cdot 10^{-6}$	$7.6 \cdot 10^{-6}$
Hardness (Mho)	5	5.7	4
Hygroscopicity	No	No	No

[a] Within parentheses is the manufacturer-provided value for the specific crystal used in our experiments [27].

2. Materials and Methods

In an attempt to determine ZnSe: Te crystal's applicability as a scintillator under X-ray radiography conditions, we concentrated our efforts on extracting and comparing a series of luminescence and scintillation properties.

A single crystal, cubic-shaped, edge 10 mm, with polished surfaces was obtained from Advatech [27]. Energy absorption efficiency (EAE), detective quantum efficiency (DQE), absolute luminescence efficiency (AE or LE), spectral matching factors (SMF), as well as effective efficiencies (EE) with various detectors were determined and compared with previously published data for GSO:Ce and BGO crystals of the same form [9]. The measurements were performed under polyenergetic X-ray excitation by a BMI Merate X-ray tube, in the range of 50–130 kVp, while keeping the current-time product at 63 mAs. Except from the tube's inherent filtration, equivalent to 2 mm Al, another 20 mm of Al were added in order to account for the attenuation by a typical human chest [32].

The energy absorption efficiency was determined as a function of different kVp of the X-ray tube. It is a measure of the energy absorbed locally, used for projection imaging detectors. This parameter is the fraction of incident X-ray energy absorbed locally at the points of X-rays interaction within the scintillator used in projection imaging detectors. This is an indication of what fraction of the incident X-ray photons contributes to the output signal formation and is expressed by [33]:

$$EAE(E) = \frac{\int_0^{E_0} \Phi_0(E) E \left(\frac{\mu_{en}(E)/\rho}{\mu_{att}(E)/\rho} \right) \left(1 - e^{-(\mu_{att}(E)/\rho)dW} \right) dE}{\int_0^{E_0} \Phi_0(E) E dE},$$

where $\Phi_0(E)$ is the X-ray photon fluence (photons per unit of area) incident on the scintillator, multiplied by the corresponding photon energy (E), giving the incident X-ray energy fluence. $\mu_{att}(E)/\rho$ is the X-ray total mass attenuation coefficient and $\mu_{en}(E)/\rho$ is the total energy absorption mass attenuation coefficient. W denotes crystal thickness (equal to 10 mm) and d is the density (in g/cm^3) [34,35].

Signal-to-noise ratio (SNR) and detective quantum efficiency (DQE), related to absorbed X-rays and optical photons have been previously investigated by Swank [36,37], under monoenergetic X-ray radiation, in terms of the noise-equivalent absorption and the statistical factor. Input SNR for poly-energetic X-ray radiation was first investigated by Nishikawa and Yaffe [38]. Dick and Motz [39] and Ginzburg and Dick [40] have also experimentally measured zero-frequency DQE under monoenergetic radiation for commercial rare earth screens. In this study, the input SNR^2, the absorbed

SNR^2, and the absorbed DQE (at zero-frequency) for the scintillators under investigation were modelled for use in the energy range of 50–130 kVp.

For energy integrated detectors, Equation (2) was used to model the input SNR^2 [36–43]:

$$SNR_{in}^2(E) = \frac{\left[\int_0^{E_0} \Psi_0(E)EdE\right]^2}{\int_0^{E_0} \Psi_0(E)E^2 dE}, \tag{2}$$

where $\Psi_0(E) = \Phi_0(E)E$ for each energy value. The numerator is equal to the square of the first statistical moment of the distribution of X-ray energy. This distribution is expressed by the X-ray spectral distribution of $\Psi_0(E)$. This is also equal to the square of the total incident X-ray energy fluence (input signal) times energy. The denominator is equal to the second moment of the aforementioned distribution, which has been considered to express the noise of the input energy fluence.

The SNR^2 of absorbed X-ray energy fluence indicates the SNR^2 of the X-ray energy fluence which is absorbed (i.e., detected) by the scintillator. It can be calculated from Equation (3) [41–43]:

$$SNR_{abs}^2(E) = \frac{\left[\int_0^{E_0} \Psi_0 EAE(E)EdE\right]^2}{\int_0^{E_0} \Psi_0 EAE(E)E^2 dE} \tag{3}$$

The detective quantum efficiency of absorbed X-rays (DQE$_{abs}$) describes the degradation of the SNR from the input to absorption within the scintillator mass. It shows the fraction of input X-ray energy fluence effectively absorbed by the scintillator. DQE$_{abs}$ may be expressed as follows [39–43]:

$$DQE_{abs}(E) = \frac{SNR_{abs}^2(E)}{SNR_{in}^2(E)} \tag{4}$$

The absolute luminescence efficiency is a measure of how much light the crystal emits (expressed as light energy flux $\dot{\Psi}_\lambda$, units $\mu W\ m^{-2}$) for a given X-ray exposure rate incident on it ($\dot{X}$, units $mR\ s^{-1}$) and is expressed in efficiency units, EU = $\mu W\ m^{-2}/(mR\ s^{-1})$ [33]. Obviously, preference is given to scintillators that achieve high AE values, thus tending to decrease the patient radiation dose.

In our experimental setup, the crystal was placed at a surface—tube focal spot distance of 72.5 cm. A dosimeter (RTI Piranha P100B) located at the same distance was used to provide the exposure rate values. For the emitted light flux, a photomultiplier tube (PMT) was used (EMI 9798 with extended sensitivity S20 photocathode), coupled to the crystal's "back" surface via a light integrating sphere (Oriel 70451), in order to minimize errors arising from light non-uniformities. No high voltage and voltage divider were used to bias the dynodes, since the PMT was connected as a biased photodiode (22 V between photocathode and the first dynode), whose current was measured by a femtoamp meter (Keithley 6430) [31].

AE is given by Equation (5) [44]:

$$AE = \eta_A = \frac{\dot{\Psi}_\lambda}{\dot{X}} = \left(\frac{i_{elec}}{S\eta_p \alpha_s c_g}\right)\dot{X}^{-1}, \tag{5}$$

where i_{elec} is the electrometer's output current in pA, S is the irradiated crystal's surface in mm^2 and η_p is the photocathode's peak photosensitivity expressed in pA/W. α_s is the spectral compatibility factor expressing the compatibility of the scintillator's emission spectrum to the spectral sensitivity of the photocathode. c_g is the geometric light collection efficiency of the experimental setup, expressing the fraction of the crystal's emitted light that impinges eventually on the PMT entrance window, after passing through the integrating sphere. The value of 15.6 was estimated for our specific setup. Concluding, AE is expressed in units of $\mu W\ m^{-2}/mR\ s^{-1}$, where $\mu W\ m^{-2}$ corresponds to the light

energy flux ($\dot{\Psi}_\lambda$) and mR s^{-1} to the exposure rate ($\dot{X}$). For simplicity, the notation efficiency unit (EU) was used: 1 EU = 1 μW m^{-2}/(mR s^{-1}).

AE is an efficiency measure of the scintillator itself, but when it comes to incorporating it in a complete system, it is the effective efficiency that better describes the system's performance, taking into consideration the light detector's spectral response. It is the product of absolute efficiency with the spectral matching factor [34,45]:

$$EE = \eta_{\text{eff}} = \eta_A \, \alpha_s, \tag{6}$$

where α_s is the spectral matching factor of the optical detector, which is given by:

$$SMF = \alpha_s = \frac{\int S_p(\lambda)S_D(\lambda)d\lambda}{\int S_p(\lambda)d\lambda}, \tag{7}$$

where S_p is the spectrum of the light emitted by the scintillator, S_D is the spectral sensitivity of the optical photon detector, and λ denotes photon wavelength [34].

The crystal's emission spectrum was obtained from Ryzhikov et.al [16]. For the sake of completeness, a variety of popular light detectors were considered; spectra extracted from their datasheets [46–49].

3. Results and Discussion

The EAE for all three crystals is plotted versus the selected kVp in Figure 1. The attenuation coefficients used in Equation (1) were calculated from the respective elementary ones (derived from the NIST XmuDat database [50,51]) and are drawn in Figure 2 for all three materials. Shown in Figure 3 is the ratio of the attenuation coefficients $\mu_{\text{en}}/\mu_{\text{att}}$ that appears in Equation (1), as a function of photon energy.
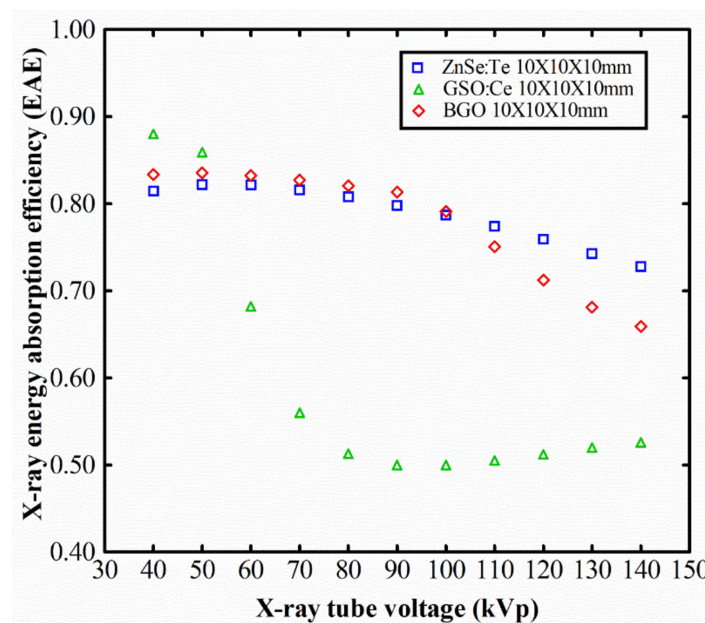

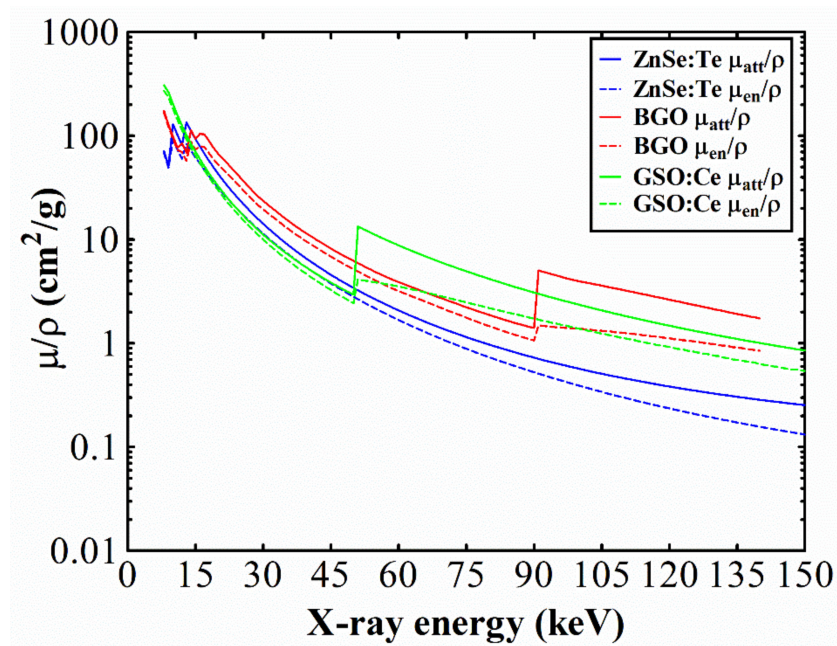**Figure 1.** Energy absorption efficiency of ZnSe: Te, BGO and GSO: Ce.

Figure 2. Attenuation coefficients of ZnSe: Te, BGO and GSO: Ce.
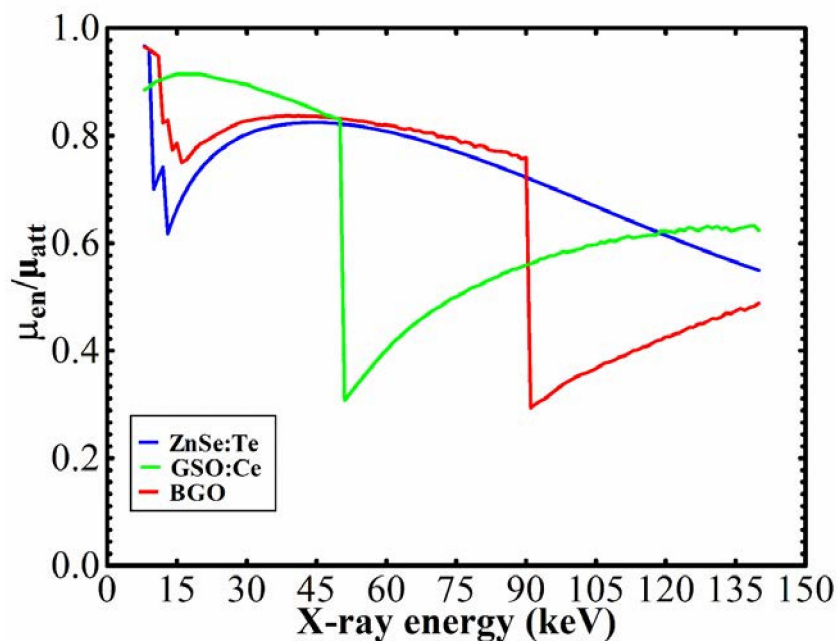

Figure 3. Attenuation coefficients ratio μ_{en}/μ_{att} of ZnSe:Te, BGO and GSO: Ce.

Decreasing of EAE while the tube voltage increases is generally obvious in Figure 1. The ability of a crystal to absorb the incident X-ray energy is expressed by μ_{att} (the probability that a photon is absorbed by the crystal, via any interaction mechanism), but more importantly by μ_{en} (the probability that a photon's energy is imparted to electrons within the material). With increasing of the tube high-voltage, the emitted X-ray spectrum shifts to higher energy regions. In these regions the attenuation coefficients generally diminish, with the exception of some areas, characteristic for every material, where the probability of photoelectric interaction maximizes locally (Figure 2), namely the K-edge, L-edge, etc. The K-edges, characteristic for GSO and BGO are found at 50.2 keV and 90.5 keV respectively, whereas ZnSe has K-edges outside the region of interest (below 13 keV, where photons have been attenuated by the Al filter). However, both GSO and BGO, at their respective K-edge

energies, exhibit a ratio μ_{en}/μ_{att} sink of more than 60%. This K-edge sink contributes to the abrupt EAE loss of GSO which is observed in Figure 1 from 60 kVp onwards. Conversely, at 40 and 50 kVp the EAE of GSO is slightly higher than that of the other two crystals, in accordance with the ratio μ_{en}/μ_{att} before the K-edge sink. At tube voltages higher than 90 kVp, there is an increasing tendency for EAE of GSO and this can be attributed to the gradual recovery of the ratio μ_{en}/μ_{att} after the K-edge energy.

On the other hand, from Figure 1 it is clear that ZnSe and BGO have a commensurate efficiency in absorbing energy, both retaining values above 0.8 up to 100 kVp and consecutively showing a gradual decrease. ZnSe exhibits a slightly lower efficiency than BGO in tube voltages up to 100 kVp, but this behavior is reversed thereafter; yet, their difference is always below 0.1. This reverse beyond 100 kVp can be attributed to the fact that μ_{en}/μ_{att} of BGO has a K-edge sink at energies pertaining to X-ray spectra obtained with tube voltages from 100 kVp to 140 kVp (i.e., 90.5 keV), whereas ZnSe does not.

Figure 4 shows the variation of input SNR^2 with X-ray tube voltage in the range 50–130 kVp. Data shown in this figure were calculated for $\Psi_0(E)$ and constant Air Kerma. The SNR^2 increases as a function of tube voltage because it depends on the product $\Psi_0(E)$ times energy.
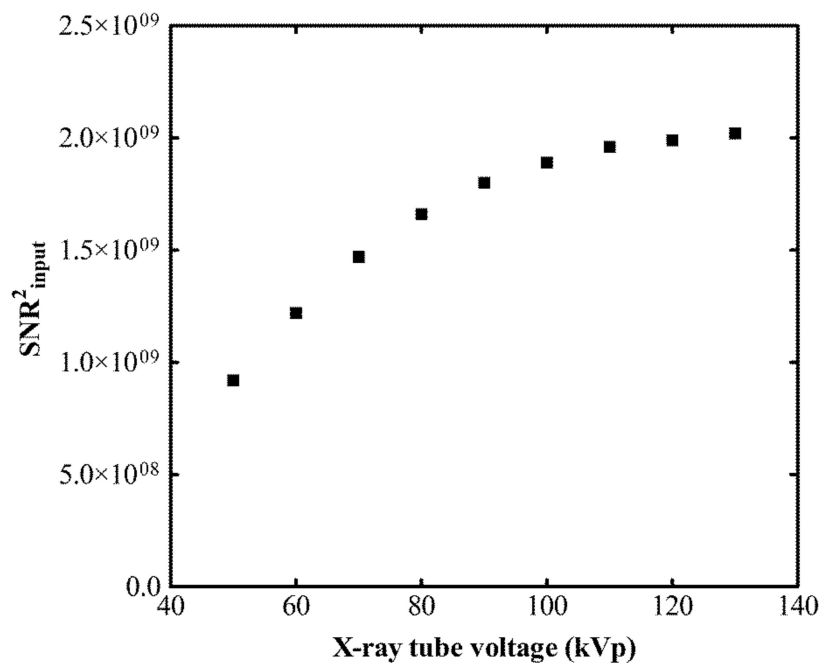

Figure 4. Signal-to-noise-ratio squared input as a function of tube voltage.

Figure 5 is a plot of the variation of SNR_{abs}^2 with X-ray tube voltage for the investigated scintillators of the same thickness. All data have been calculated using energy fluence for constant Air Kerma. The calculated results depend on the EAE of the scintillators (see Figure 1). ZnSe:Te demonstrates the maximum SNR_{abs}^2 values, especially at high tube voltages (more than 110 kVp).
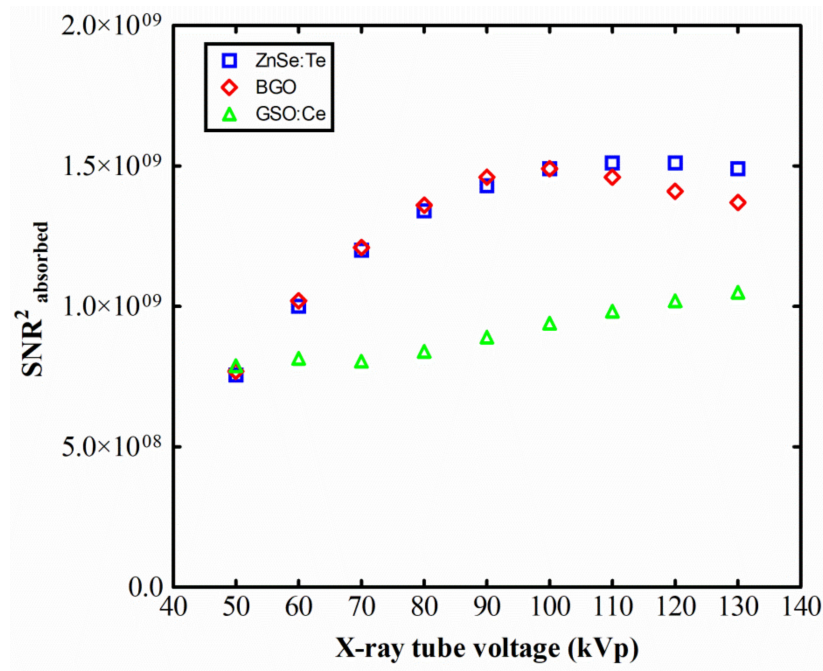
Figure 5. Signal-to-noise ratio squared absorbed of ZnSe: Te, BGO and GSO: Ce.

The DQE absorbed values as a function of set tube voltage for the three crystals are shown in Figure 6, which also demonstrates that for all scintillators the DQE absorbed values are equal to EAE (see Figure 1). Again, ZnSe:Te demonstrates the highest DQE absorbed values at high tube voltages (more than 110 kVp).
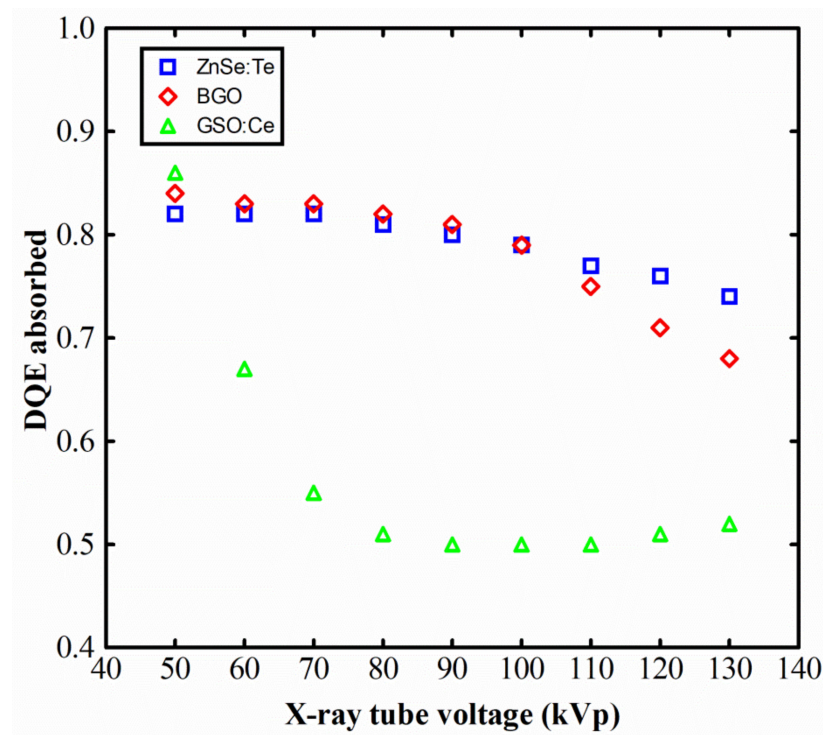

Figure 6. Detective quantum efficiency absorbed of ZnSe: Te, BGO and GSO: Ce.

Absolute luminescence efficiency values for the three crystals as a function of the set tube high-voltage are presented in Figure 7.
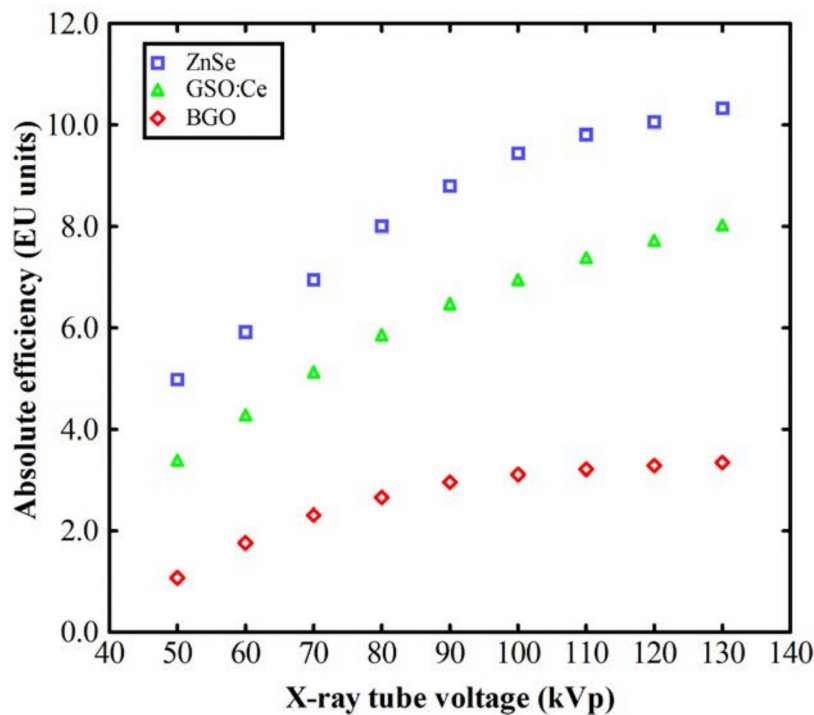
Figure 7. Luminescence efficiency of the ZnSe:Te single crystal. Comparison with BGO and GSO:Ce.

All three materials exhibit a constantly increasing AE with increasing of the kVp, but ZnSe: Te clearly outperforms having at least 2 EU higher than GSO: Ce and 4–7 EU higher than BGO, in every point of the graph. Obvious is the proportionality between AE and kVp for both ZnSe:Te and GSO:Ce in the tube high-voltage region from 50–80 kVp. At higher voltages, the relation is non-proportional, something that Balcerzyk et al. [11] attribute to the crystal's structure, as far as GSO: Ce is concerned.

Revisiting the remark expressed in the introductory section, that the material's light yield varies within a broad interval [18], one can note that it still remains higher than the values reported for BGO and GSO:Ce, even in its "least efficient" version (see Table 1, footer note). This is verified by the AE-kVp graph, even though ZnSe: Te has lower density and effective atomic number than the other ones.

Specifically, at the end of its proportionality region, i.e., 80 kVp, ZnSe: Te attains a value of 8 EU, as opposed to the 5.8 EU of GSO: Ce and the 2.6 EU of BGO. At the highest tube voltage applied in our experiments, 130 kVp, the absolute efficiency differences were even greater, measuring 10.4 EU, 8 EU and 3.3 EU respectively. Also prominent in the same graph is the non-proportional behavior of BGO in the whole energy region examined herein, as well as the plateau that it exhibits above 100 kVp, with the AE value stabilizing below 3.3 EU.

The linear relationship between light output and exposure rate is depicted in Figure 8 for all three materials. Linear interpolation lines have been drawn for the data points, with the R^2 value (i.e., the coefficient of determination) being at least 0.996 in any case. The lines' slopes come in agreement with the relationship between the three crystals' AE values (Figure 7). The higher slope of the ZnSe: Te line corresponds to higher AE values, whereas the other two materials stand lower, with GSO: Ce slope being closer to that of ZnSe: Te.

In Figures 9 and 10, the emitted spectrum of ZnSe: Te [16], is juxtaposed with the spectral responses of several commercially available detectors. For ease of comparison, everything is normalized. Luminescence of ZnSe: Te peaks at 640 nm [16].
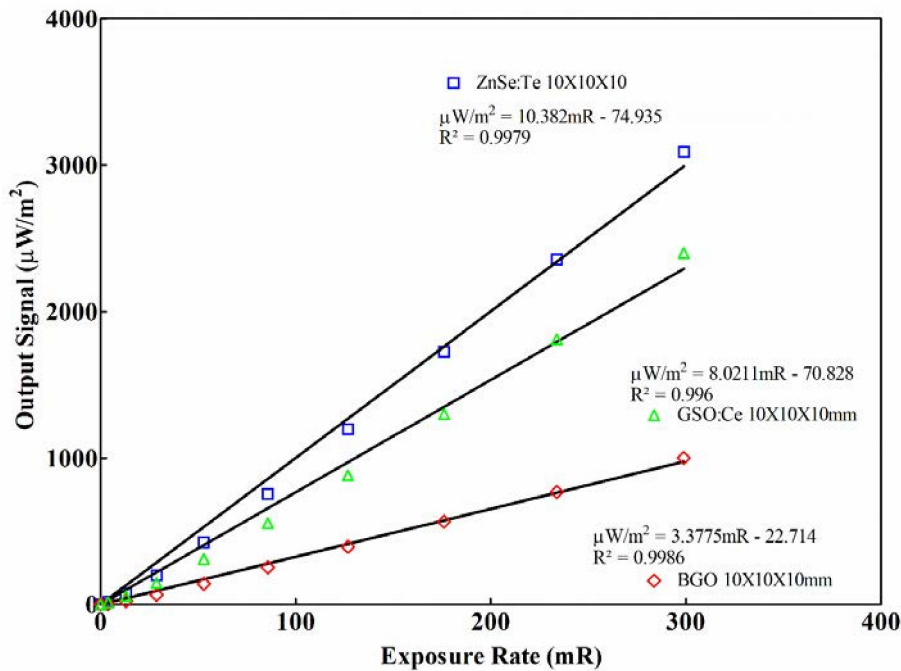
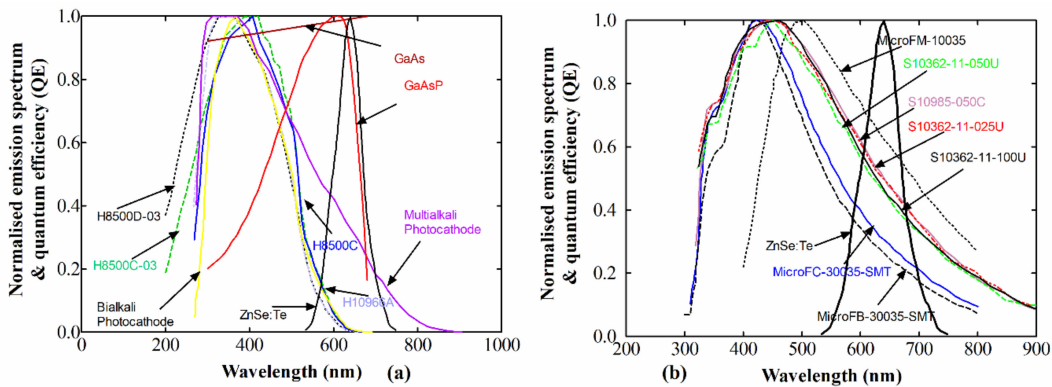**Figure 8.** Output signal of the ZnSe: Te, BGO and GSO: Ce crystals.

Figure 9. Normalized emission spectrum of ZnSe:Te in comparison with the spectral sensitivities of various sensors: (**a**) photocathodes; (**b**) silicon photomultipliers.
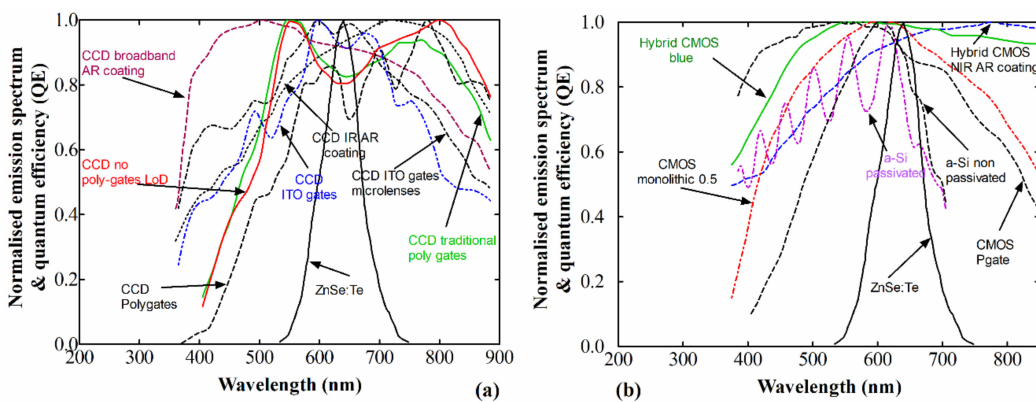

Figure 10. Normalized emission spectrum of ZnSe:Te in comparison with the spectral sensitivities of various sensors: (**a**) charge-coupled-devices; (**b**) complementary metal-oxide semiconductors.

From Table 2, that summarizes the SMF with every such detector, comes out the perfect match that takes place between this crystal and several CCD and CMOS detectors, a fact that verdicts towards

the usability of ZnSe: Te in digital X-ray systems. A nearly total overlap, above 0.96, is found with the monolithic 0.25μm CMOS and the CMOS RadEye high resolution that are currently used in a number of commercial radiography systems, both industrial and medical. Mediocre compatibility instead was registered with the PMT EMI 9798 extended photocathode (E–S20) used in our experiments, since the SMF was only 0.60. In any case, this value is taken into consideration for the latter calculations.

Table 2. ZnSe: Te Spectral matching factors with commercially available detectors.

Optical Detectors	ZnSe:Te	Optical Detectors	ZnSe:Te
CCD broadband AR coating	0.91	GaAsP phosphor photocathode	0.79
CCD infrared (IR) anti-reflection (AR) coating	0.92	Extended photocathode (E-S20)	0.60
CMOS hybrid, blue anti-reflection (AR) coating	0.94	Si PM MicroFC-30035-SMT	0.34
Hybrid CMOS blue	0.99	Si PM MicroFB-30035-SMT	0.30
CMOS (monolithic 0.25μm)	0.96	Si PM MicroFM-10035	0.67
a-Si:H passivated	0.77	Si PM S10985-050C	0.55
a-Si:H non-passivated	0.85	Si PM S10362-11-025U	0.54
CCD indium tin oxide (ITO) gates, microlenses	0.96	Si PM S10362-11-050U	0.55
CCD with indium tin oxide (ITO) gates	0.90	Si PM S10362-11-100U	0.52
CCD with polygates	0.78	Flat panel PS-PMT H8500C-03	0.08
CCD no poly-gates LoD	0.87	Flat panel PS-PMT H8500D-03	0.05
CCD with traditional poly gates	0.88	Flat panel PS-PMT H10966A	0.05
CMOS (photogate array 0.5)	0.91	Flat panel PS-PMT H8500C	0.07
CMOS RadEye HR	0.97	Bialkali Photocathode	0.06
GaAs Photocathode	0.99	Multialkali Photocathode	0.36

More tangible data regarding this "usability", provide the EE values. These are plotted versus tube's kVp in Figure 11 for every detector mentioned before and verify the perfect compatibility with several of them. EE values nearly equal to the AE ones are obtained (~5 EU at 50 kVp and ~10 EU at 130 kVp) when ZnSe: Te is combined, e.g., with the CMOS hybrid blue sensor, the CCD with ITO gates and microlenses, the GaAs photocathode, in addition to the two above-mentioned commercial CMOS.
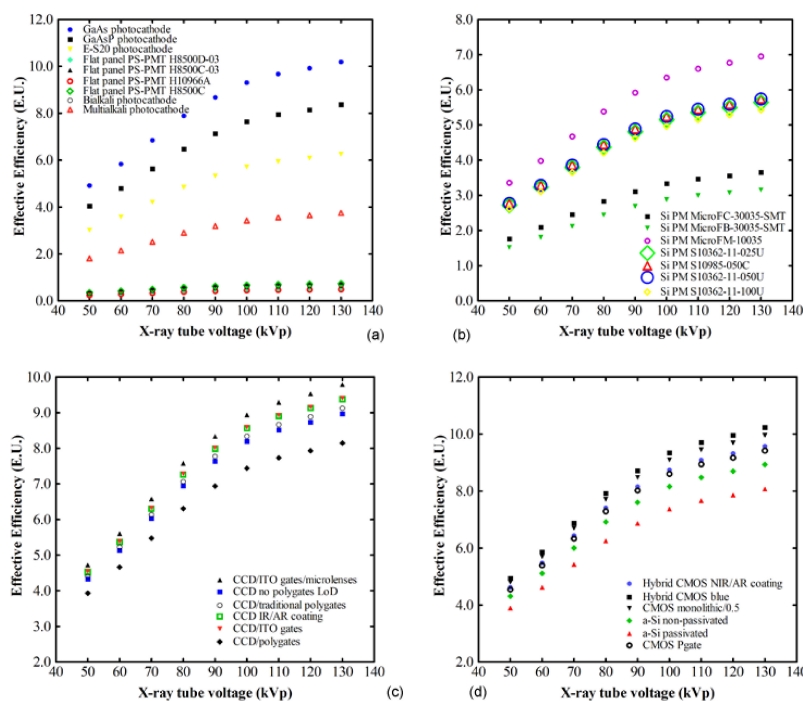
Figure 11. Effective luminescence efficiencies of ZnSe: Te combined with various sensors: (**a**) photocathodes; (**b**) silicon photomultipliers; (**c**) charge-coupled-devices; (**d**) complementary metal-oxide semiconductors.

4. Conclusions

The output luminescence signal of a ZnSe: Te single crystal was examined within the radiographic energy region for possible applications in novel radiographic applications (such as dual energy). To this aim, the spectral compatibility with various commercial sensors was also considered. BGO and GSO: Ce crystals of equal dimensions were used, for the purpose of comparison. In terms of EAE and DQEabs, both ZnSe and BGO demonstrated commensurate performance, especially in tube voltages up to 100 kVp. The maximum luminescence efficiency was obtained at the maximum examined X-ray energy (130 kVp) since the light output of ZnSe: Te constantly increased within the energy range in question. The emitted optical photons of ZnSe: Te were found to be optimally detected by a wide range of complementary metal–oxide–semiconductors (CMOS), photocathodes, and charge-coupled-devices (CCD). These properties, together with those mentioned in the introductory section (brief decay times and convenient filtering capabilities), qualify the use of ZnSe: Te as a high spectral energy photon absorber in dual-energy arrays, improving the overall detection capability.

References

1.　Kandarakis, I.S. Luminescence in medical image science. *J. Lumin.* **2016**, *169*, 553–558. [CrossRef]
2.　Lecoq, P.; Gektin, A.; Korzhik, M.; Pedrini, C. *Inorganic Scintillators for Detector Systems: Physical Principles and Crystal Engineering*; Lecoq, P., Ed.; Particle acceleration and detection; Springer: Berlin/Heidelberg, Germany, 2006; ISBN 978-3-540-27766-8.
3.　Bizarri, G.; Moses, W.W.; Singh, J.; Vasil'ev, A.N.; Williams, R.T. An analytical model of nonproportional scintillator light yield in terms of recombination rates. *J. Appl. Phys.* **2009**, *105*, 044507. [CrossRef]
4.　Jaffe, J.E.; Jordan, D.V.; Peurrung, A.J. Energy nonlinearity in radiation detection materials: Causes and consequences. *Nucl. Instrum. Methods Phys. Res. Sect. A Accel. Spectrometers Detect. Assoc. Equip.* **2007**, *570*, 72–83. [CrossRef]
5.　Van Eijk, C.W.E. Inorganic-scintillator development. *Nucl. Instrum. Methods Phys. Res. Sect. A Accel. Spectrometers Detect. Assoc. Equip.* **2001**, *460*, 1–14. [CrossRef]
6.　Hofstadter, R. The Detection of Gamma-Rays with Thallium-Activated Sodium Iodide Crystals. *Phys. Rev.* **1949**, *75*, 796–810. [CrossRef]
7.　Grassmann, H.; Lorenz, E.; Moser, H.G. Properties of CsI(TI)—Renaissance of an old scintillation material. *Nucl. Instrum. Methods Phys. Res. Sect. A Accel. Spectrometers Detect. Assoc. Equip.* **1985**, *228*, 323–326. [CrossRef]
8.　Jagtap, S.; Chopade, P.; Tadepalli, S.; Bhalerao, A.; Gosavi, S. A review on the progress of ZnSe as inorganic scintillator. *Opto-Electron. Rev.* **2019**, *27*, 90–103. [CrossRef]
9.　Valais, I.; Michail, C.; David, S.; Nomicos, C.D.; Panayiotakis, G.S.; Kandarakis, I. A comparative study of the luminescence properties of LYSO: Ce, LSO: Ce, GSO: Ce and BGO single crystal scintillators for use in medical X-ray imaging. *Phys. Med.* **2008**, *24*, 122–125. [CrossRef] [PubMed]
10.　Van Eijk, C.W.E. Inorganic scintillators in medical imaging. *Phys. Med. Biol.* **2002**, *47*, R85–R106. [CrossRef]
11.　Balcerzyk, M.; Moszynski, M.; Kapusta, M.; Wolski, D.; Pawelke, J.; Melcher, C.L. YSO, LSO, GSO and LGSO. A study of energy resolution and nonproportionality. *IEEE Trans. Nucl. Sci.* **2000**, *47*, 1319–1323. [CrossRef]
12.　Kozma, P.; Kozma, P. Radiation sensitivity of GSO and LSO scintillation detectors. *Nucl. Instrum. Methods Phys. Res. Sect. A Accel. Spectrometers Detect. Assoc. Equip.* **2005**, *539*, 132–136. [CrossRef]

13. Holl, I.; Lorenz, E.; Mageras, G. A measurement of the light yield of common inorganic scintillators. *Ieee Trans. Nucl. Sci.* **1988**, *35*, 105–109. [CrossRef]

14. Ryzhikov, V.; Chernikov, V.; Gal'chinetskii, L.; Galkin, S.; Lisetskaya, E.; Opolonin, A.; Volkov, V. The use of semiconductor scintillation crystals II-VI in radiation instruments. *J. Cryst. Growth* **1999**, *197*, 655–658. [CrossRef]

15. Atroshchenko, L.V.; Gal'chinetskii, L.P.; Galkin, S.N.; Ryzhikov, V.D.; Silin, V.I.; Shevtsov, N.I. Distribution of tellurium in melt-grown ZnSe(Te) crystals. *J. Cryst. Growth* **1999**, *197*, 471–474. [CrossRef]

16. Ryzhikov, V.; Grinyov, B.; Galkin, S.; Starzhinskiy, N.; Rybalka, I. Growing technology and luminescent characteristics of ZnSe doped crystals. *J. Cryst. Growth* **2013**, *364*, 111–117. [CrossRef]

17. Dafinei, I.; Nagorny, S.; Pirro, S.; Cardani, L.; Clemenza, M.; Ferroni, F.; Laubenstein, M.; Nisi, S.; Pattavina, L.; Schaeffner, K.; et al. Production of ^{82}Se enriched Zinc Selenide (ZnSe) crystals for the study of neutrinoless double beta decay. *J. Cryst. Growth* **2017**, *475*, 158–170. [CrossRef]

18. Cool, S.; Miller, S.; Brecher, C.; Lingertat, H.; Sarin, V.; Riley, K.; Mashl, S.; Tylus, P.; Nagarkar, V. Fabrication of ZnSe: Te by hot pressing techniques. In Proceedings of the 2009 IEEE Nuclear Science Symposium Conference Record (NSS/MIC), Orlando, FL, USA, 25–31 October 2010; pp. 2441–2447.

19. Gaysinskiy, V.; Singh, B.; Ovechkina, L.; Miller, S.; Thacker, S.; Nagarkar, V. Luminescence Properties and Morphology of ZnSe: Te Films. *IEEE Trans. Nucl. Sci.* **2008**, *55*, 1556–1560. [CrossRef]

20. Cho, Y.H.; Park, S.H.; Lee, W.G.; Ha, J.H.; Kim, H.S.; Starzinskiy, N.; Lee, D.H.; Park, S.; Kim, Y.K. Comparative Study of a CsI and a ZnSe(Te/O) Scintillation Detector's Properties for a Gamma-ray Measurement. *J. Nucl. Sci. Technol.* **2008**, *45*, 534–537. [CrossRef]

21. Passeri, A.; Formiconi, A.R. Lu$_2$SiO$_5$: Ce. In *Ionizing Radiation Detectors for Medical Imaging*; Guerra, A.D., Ed.; WORLD SCIENTIFIC: Hackensack, NJ, USA, 2004; p. 256. ISBN 978-981-238-674-8.

22. Christian, J. Advances in CMOS SSPM Detectors. In *Biological and Medical Sensor Technologies*; Iniewski, K., Ed.; CRC Press: Boca Raton, FL, USA, 2017; p. 327. ISBN 978-1-138-07321-0.

23. Stolberg-Rohr, T.; Hawkins, G.J. Spectral design of temperature-invariant narrow bandpass filters for the mid-infrared. *Opt. Express* **2015**, *23*, 580. [CrossRef]

24. Rodnyj, P.A. Interaction of Ionizing Radiation with Scintillators. In *Physical Processes in Inorganic Scintillators*; The CRC Press Laser and Optical Science and Technology Series; CRC Press: Boca Raton, FL, USA, 1997; p. 17. ISBN 978-0-8493-3788-8.

25. Mateck Zinc Selenide, ZnSe. Available online: http://www.matweb.com/search/datasheet.aspx?matguid=fb891a04b5bc46d1832fbb5906d9190c&ckck=1 (accessed on 7 January 2020).

26. Grinyov, B.; Ryzhikov, V.; Lecoq, P.; Naydenov, S.; Opolonin, A.; Lisetskaya, E.; Galkin, S.; Shumeiko, N. Dual-energy radiography of bone tissues using ZnSe-based scintielectronic detectors. *Nucl. Instrum. Methods Phys. Res. Sect. A Accel. Spectrometers Detect. Assoc. Equip.* **2007**, *571*, 399–403. [CrossRef]

27. Advatech UK. ZnSe:Te. Available online: https://www.advatech-uk.co.uk/znse_te.html (accessed on 15 June 2020).

28. Ryzhikov, V.D.; Naydenov, S.V.; Onyshchenko, G.M.; Lecoq, P.; Smith, C.F. A spectrometric approach in radiography for detection of materials by their effective atomic number. *Nucl. Instrum. Methods Phys. Res. Sect. A Accel. Spectrometers Detect. Assoc. Equip.* **2009**, *603*, 349–354. [CrossRef]

29. Martini, N.; Koukou, V.; Fountos, G.; Michail, C.; Bakas, A.; Kandarakis, I.; Speller, R.; Nikiforidis, G. Characterization of breast calcification types using dual energy x-ray method. *Phys. Med. Biol.* **2017**, *62*, 7741–7764. [CrossRef] [PubMed]

30. Martini, N.; Koukou, V.; Michail, C.; Fountos, G. Dual Energy X-ray Methods for the Characterization, Quantification and Imaging of Calcification Minerals and Masses in Breast. *Crystals* **2020**, *10*, 198. [CrossRef]

31. Saatsakis, G.; Kalyvas, N.; Michail, C.; Ninos, K.; Bakas, A.; Fountzoula, C.; Sianoudis, I.; Karpetas, G.E.; Fountos, G.; Kandarakis, I.; et al. Optical Characteristics of ZnCuInS/ZnS (Core/Shell) Nanocrystal Flexible Films Under X-Ray Excitation. *Crystals* **2019**, *9*, 343. [CrossRef]

32. Michail, C.; Valais, I.; Martini, N.; Koukou, V.; Kalyvas, N.; Bakas, A.; Kandarakis, I.; Fountos, G. Determination of the detective quantum efficiency (DQE) of CMOS/CsI imaging detectors following the novel IEC 62220-1-1:2015 International Standard. *Radiat. Meas.* **2016**, *94*, 8–17. [CrossRef]

33. Michail, C.; Koukou, V.; Martini, N.; Saatsakis, G.; Kalyvas, N.; Bakas, A.; Kandarakis, I.; Fountos, G.; Panayiotakis, G.; Valais, I. Luminescence Efficiency of Cadmium Tungstate (CdWO$_4$) Single Crystal for Medical Imaging Applications. *Crystals* **2020**, *10*, 429. [CrossRef]

34. Michail, C.; Valais, I.; Fountos, G.; Bakas, A.; Fountzoula, C.; Kalyvas, N.; Karabotsos, A.; Sianoudis, I.; Kandarakis, I. Luminescence efficiency of calcium tungstate ($CaWO_4$) under X-ray radiation: Comparison with Gd_2O_2S:Tb. *Measurement* **2018**, *120*, 213–220. [CrossRef]

35. Boone, J. X-ray production, interaction, and detection in diagnostic imaging. In *Handbook of Medical Imaging. Volume 1: Physics and Psychophysics*; Beutel, J., Kundel, H.L., Van Metter, R.L., Eds.; SPIE Press: Bellingham, WA, USA, 2000; Volume 1, pp. 36–57. ISBN 978-0-8194-7772-9.

36. Swank, R.K. Calculation of Modulation Transfer Functions of X-Ray Fluorescent Screens. *Appl. Opt.* **1973**, *12*, 1865. [CrossRef]

37. Swank, R.K. Absorption and noise in X-ray phosphors. *J. Appl. Phys.* **1973**, *44*, 4199–4203. [CrossRef]

38. Nishikawa, R.M.; Yaffe, M.J. Signal-to-noise properties of mammographic film-screen systems: SNR properties of mammographic film-screen systems. *Med. Phys.* **1985**, *12*, 32–39. [CrossRef]

39. Dick, C.E.; Motz, J.W. Image information transfer properties of X-ray fluorescent screens. *Med. Phys.* **1981**, *8*, 337–346. [CrossRef] [PubMed]

40. Ginzburg, A.; Dick, C.E. Image information transfer properties of x-ray intensifying screens in the energy range from 17 to 320 keV. *Med. Phys.* **1993**, *20*, 1013–1021. [CrossRef] [PubMed]

41. Konstantinidis, A. Predicted image quality of a CMOS APS X-ray detector across a range of mammographic beam qualities. *J. Phys. Conf. Ser.* **2015**, *637*, 012012. [CrossRef]

42. Konstantinidis, A. Physical Parameters of Image Quality. In *Comprehensive Biomedical Physics*; Elsevier: Amsterdam, The Netherlands, 2014; pp. 49–63. ISBN 978-0-444-53633-4.

43. Konstantinidis, A.C.; Szafraniec, M.B.; Speller, R.D.; Olivo, A. The Dexela 2923 CMOS X-ray detector: A flat panel detector based on CMOS active pixel sensors for medical imaging applications. *Nucl. Instrum. Methods Phys. Res. Sect. AAccel. SpectrometersDetect. Assoc. Equip.* **2012**, *689*, 12–21. [CrossRef]

44. Michail, C.; Ninos, K.; Kalyvas, N.; Bakas, A.; Saatsakis, G.; Fountos, G.; Sianoudis, I.; Panayiotakis, G.; Kandarakis, I.; Valais, I. Spectral efficiency of lutetium aluminum garnet ($Lu_3Al_5O_{12}$:Ce) with microelectronic optical sensors. *Microelectron. Reliab.* **2020**, *109*, 113658. [CrossRef]

45. Valais, I.G.; Kandarakis, I.S.; Nikolopoulos, D.N.; Sianoudis, I.A.; Dimitropoulos, N.; Cavouras, D.A.; Nomicos, C.D.; Panayiotakis, G.S. Luminescence efficiency of (Gd_2SiO_5:Ce) scintillator under x-ray excitation. In Proceedings of the IEEE Symposium Conference Record Nuclear Science 2004, Rome, Italy, 16–22 October 2004; Volume 5, pp. 2737–2741.

46. Hamamatsu Photonics, MPPC (Multi-Pixel Photon Counters). Available online: https://www.hamamatsu.com/eu/en/product/optical-sensors/mppc/index.html (accessed on 29 June 2020).

47. Magnan, P. Detection of visible photons in CCD and CMOS: A comparative view. *Nucl. Instrum. Methods Phys. Res. Sect. A Accel. Spectrometers Detect. Assoc. Equip.* **2003**, *504*, 199–212. [CrossRef]

48. Rowlands, J.A.; Yorkston, J. Flat Panel Detectors for Digital Radiography. In *Handbook of Medical Imaging. Volume 1: Physics and Psychophysics*; Beutel, J., Kundel, H.L., Van Metter, R.L., Eds.; SPIE Press: Bellingham, WA, USA, 2000; Volume 1, pp. 223–328. ISBN 978-0-8194-7772-9.

49. Silicon Photomultipliers (SiPM). Available online: https://www.onsemi.com/products/sensors/silicon-photomultipliers-sipm (accessed on 29 June 2020).

50. Storm, L.; Israel, H.I. Photon cross sections from 1 keV to 100 MeV for elements $Z = 1$ to $Z = 100$. *At. Data Nucl. Data Tables* **1970**, *7*, 565–681. [CrossRef]

51. Hubbell, J.H.; Seltzer, S.M. *Tables of X-Ray Mass Attenuation Coefficients and Mass Energy-Absorption Coefficients, NIST Standard Reference Database 126*; National Institute of Standards and Technology (NIST): Gaithersburg, MD, USA, 1995.